The effects of microstructures and repassivation kinetics on the tribocorrosion resistance of ferrite and ferrite-martensite stainless steels

V. Dalbert, N. Mary, Bernard Normand, C. Verdu, Thierry Douillard, S. Saedlou

The effects of microstructures and repassivation kinetics on the tribocorrosion resistance of ferrite and ferrite-martensite stainless steels.

V. Dalbert[1] N. Mary[1,2], B. Normand[1], C. Verdu[1], T. Douillard[1], S. Saedlou[3]

1. Université de Lyon, INSA Lyon, MATEIS UMR CNRS 5510, F-69621 Villeurbanne Cedex, France

2. ELyTMaX UMI 3757, CNRS – Université de Lyon – Tohoku University, International Joint Unit, Tohoku University, Sendai, Japan

3. APERAM Research Center, rue Roger Salengro BP15, F-62330 Isbergues, France

Some highlights of this work can be given such as:

- Martensite-ferrite microstructure enhance tribocorrosion resistance by hard phase reinforcement.

- The applied potential plays a role on the contribution of the corrosion wear.

- The total wear increases even if the surface repassivation is faster at higher potential. Therefore, wear is mainly driven by the mechanical wear.

- Subsurface stain hardening increase with the repassivation kinetic increase in the dual phase microstructure.

- Dynamic recrystallization is affected by the material microstructure and mainly occurs in the softer phase

The effects of microstructures and repassivation kinetics on the tribocorrosion resistance of ferrite and ferrite-martensite stainless steels.

V. Dalbert[1] N. Mary[1,2], B. Normand[1], C. Verdu[1], T. Douillard[1], S. Saedlou[3]

1. Université de Lyon, INSA Lyon, CNRS, MATEIS UMR 5510, F-69621 Villeurbanne Cedex, France

2. ELyTMaX UMI 3757, CNRS – Université de Lyon – Tohoku University, International Joint Unit, Tohoku University, Sendai, Japan

3. APERAM Research Center, rue Roger Salengro BP15, F-62330 Isbergues, France

* corresponding author: nicolas.mary@insa-lyon.fr

Abstract

The study addresses the tribocorrosion behavior of a ferritic stainless steel and a ferrite-martensite stainless steel under two passive potentials. The dual phase microstructure was produced by a specific heat treatment applied to the ferritic stainless steel. Since both materials have the same chemical composition, their tribocorrosion resistances are discussed in terms of microstructure benefit. This benefit concerns the determination of the wear rate, as well as the identification of the wear mechanism from surface and sub-surface observations. In parallel, current transients recorded during sliding are analyzed to quantify the kinetics of repassivation and evaluate the impact of the rebuilding of oxide film on wear.

The results show that the hardness of the material is the main parameter that controls wear for the sliding conditions selected in this work. In a second order of magnitude, the nature of the oxide layer plays a role in the damage mechanism. Finally, if the oxide growth rate is affected by both the applied potential and the microstructure, it mainly affects the subsurface microstructure of the wear track with a thickening of the grain refined layer, as the repassivation is faster.

Keywords

Tribocorrosion; stainless steel, thermal treatment; repassivation; microstructure, electrochemistry

1- Introduction

Tribocorrosion experiments are usually designed to characterize the wear resistance of materials when superficial mechanical loading (tribology) and superficial electrochemical reactions act simultaneously. Among all mechanical properties considered in dry wear resistance studies [1], [2], the hardness is usually considered as a key descriptor, as reported in other works [3]–[7]. The empirical law proposed by Archard links the volume loss of matter during an unlubricated wear test to the hardness of the softest contacting surfaces and the normal load [7], [8]. Therefore, hardness is the major input parameter in the modeling of tribological behavior in wear resistance material design, especially as long as no cracks initiate and propagate under the wear track [9], [10], [5]. In this context, metallic alloys such as ferritic stainless steels are preferred for developing load transport rails and conveyers used in aggressive media or automotive mechanical parts, cooking tools, etc. [11], [12]. Their metallurgical features also allow them to achieve composite microstructures, such as dual-phase (ferrite-martensite) or duplex (ferrite-austenite) microstructures. The combination of two phases then enhances both the hardness and toughness of the material, increasing the opportunity to use them [13]. For dual phase microstructures, it has been proven that the wear rate decreases as the martensite content increases (e.g., the hard phase) in the ferrite matrix. However, this beneficial effect is expected until the distribution of the ferrite prevents the percolation of the martensite [10], [14], [15]. For Aksoy et al. [14] and Saghafian and Kheirandish [16], the maximum wear resistance increase is reached for a martensite content between 17 to 35 % in the ferrite matrix.

To better resist corrosive environments, dual phase stainless steels have been produced by steel makers. However, these materials, as all passive materials, are more sensitive to tribocorrosion. Indeed, the passive film or the oxide layer can act as a wear accelerant [17]. Their wear resistances also depend on the environmental conditions, defined by the chemical and mechanical loads. Jemmely et al. [18] demonstrated that the wear rate of a ferritic stainless steel is higher in acidic solutions compared to neutral or basic solutions because of the nature of the oxide film and the higher reactivity of the surface. Instead of varying pH, potentiostatic tests can be used in tribocorrosion experiments [9]. For pH variation, potentiostatic measurements can modify the material reactivity in terms of film

thickness, chemistry, etc., affecting the wear resistance at the end [19]. The effect of the mechanical load must also be taken into account on the oxide film because it creates debris at the point of contact, and it generates additional defects underneath the surface [20]. On the one hand, debris is either comprised of abrasive particles that increase the wear while they are in contact with the two pieces or acted as solid lubricant particles as a function of their morphologies and hardnesses [21]. On the other hand, the mechanical load generates defects such as dislocations in the subsurface [22]. A portion is annihilated due to the surface dissolution [23], while another portion is blocked by the passive film formation which provides a strain accumulation underneath the wear track [24], [25], [26]. Consequently, the stacking fault energy under plastic deformation favors dynamic recrystallization and/or grain rotation in the nearby surface and changes the subsurface mechanical properties of the material [1], [27], [28].

While addressing material optimization for tribocorrosion issues, both chemical composition and microstructure modifications need be evaluated separately. However, wear improvement usually requires their adjustments at the same time [29], [30]. In some applications, such as the food industry or orthopedic applications, some chemical elements, such as nickel, are avoided for toxicity reasons, even if they are beneficial for the wear resistance. An alternative solution consists of performing a specific heat treatment to improve the hardness and toughness of a single-phase material by promoting a dual phase microstructure, as is done on ferritic stainless steels. In this work, this solution was chosen to improve the wear resistance of a commercial 17 % Cr ferrite stainless (AISI 430F) into a ferrite-martensite stainless steel (AISI430-FM). Taking the advantage that the chemical composition of the materials is shared, the role of the microstructure on the depassivation/repassivation kinetics can be evaluated and linked to the wear behavior of the two materials.

A corundum counterpart was chosen because of its higher wear and chemistry resistances compared to the stainless steel in order to only be focused on the reactivity of the substrate. This paper presents a comparison of the tribocorrosion behavior of a mono-phase and a dual phase stainless steels with a similar chemical composition. Wear tests are performed in the passive domain for two potentials defined at the beginning and at the minimum of the current density of the passive plateau. The wear

resistances of the two materials are tested against an inert counterpart in order to focus on the stainless-steel reactivity. These latter are also described in term of wear volumes and contribution of the mechanical and corrosion wear. In addition, the passivation kinetic of the wear tracks are quantified in order to discuss its effect on the sub-surface microstructure evolution and to conclude about the effect of the microstructure on the tribochemical wear resistance.

2- Materials and experimental procedure

2.1. Heat treatments and tribocorrosion samples

To obtain a dual phase microstructure, ferrite stainless steel (AISI430-F) was first heated to 1000°C for 1 min to reach the ferrite–austenite domain and then cooled down by rapid air quenching to fix the ferrite-martensite microstructure (AISI430-FM). Consequently, both ferrite and ferrite-martensite stainless steels present the same chemical composition: 0.03 wt% C, 16.10 wt% Cr, 0.20 wt% Ni, 0.49 wt% Si, and a balance of Fe.

Disc samples of 50 mm diameter and 3 mm thickness were prepared from cold rolled sheets. Surfaces were ground with SiC emery paper up to grade 2400 and then polished with several diamond pastes down to 1 µm. After the final polishing step, the samples were cleaned in an ethanol ultrasonic bath for 1 min, then dried with pulsed dry air and finally stored for 24 h in a desiccator for native oxide film aging. In addition, to get a flat surface for corrosion and tribocorrosion testing, surface preparation removed approximately 1 mm of matter, meaning that the work hardening layer generated by the cold rolling of the sheet was suppressed (Figure 1a). Cross-section observations on AISI430-FM confirm that not only the surface but also the volume of the material were transformed after heat treatment (Figure 1b).

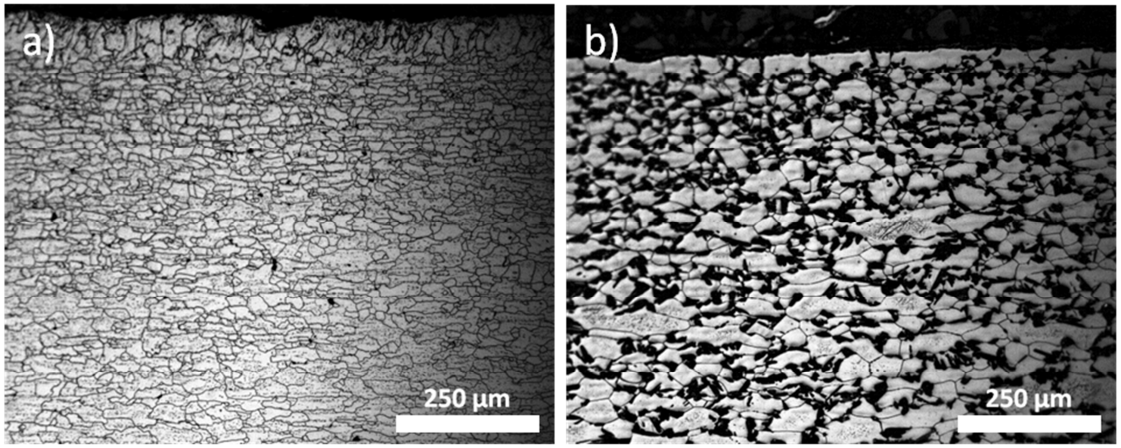

Figure 1. FE-SEM cross section observations of a) as received AISI430-F and b) AISI 430FM after chemical etching.

Before tribocorrosion, microstructural observations were made after two different electrochemical etchings; this consisted of an applied potential of 1 V (vs a steel cathode) for 45 s in a solution at 60 wt% HNO_3 for AISI430-F, whereas the AISI43-FM microstructure was revealed by soaking in 40 wt% NaOH for 1 min at 2 V vs a steel cathode.

2.2 Surface hardness characterization

Microhardness measurements were collected on polished surfaces using a Buehler MicroMet 5104 under a load of 9.8 N, maintained for 20 s. Average values were calculated from 10 indentations on each sample. These measurements were completed in nanoindentation tests using a G200 nanoindenter (Agilent Technologies). A Berkovich indenter with a 65° angle of curvature was controlled in displacement to 1 µm under the polished surface. The hardness calculation was based on the Oliver and Pharr method, using the continuous stiffness measurement (CSM) technique [31]. Only indents located in the ferrite and/or martensite phases were considered for calculating the average hardness values (20 measurements each time). This procedure was selected in order to reduce the effects of grain boundaries, carbides, etc., on the measurement and to obtain more accurate results relative to each phase hardness.

2.3. Tribocorrosion parameters and wear characterization

Tribocorrosion tests were performed using a reciprocating-motion tribometer (Falex Tribology N. V., Belgium) [30]. The experiments were duplicated at least three times. A corundum alumina pin with a curvature radius of 25 mm and diameter of 6 mm was selected as a counter body (Young's modulus and Poisson's ratio of 380 GPa and 0.25, respectively). As indicated in the introduction, this configuration was selected to strike only the wear of the stainless steels and to compare the microstructure effect. Sliding occurred for a maximum of 1000 cycles with a stroke length of 10 mm and under a nominal applied load of 10 N (i.e., total sliding distance of 20 m). A trapezoidal pin motion was applied with an acceleration of 500 $mm.s^{-2}$ and a maximum velocity of 60 $mm.s^{-1}$. The forward and backward latency periods were set at 5.7 s: 0.7 s induced by the change in direction of the pin and 5 s selected by the operator. This selection was made from preliminary experiments where the latency periods comprised between 1 s to 10 s were tested. In this work, the transient analysis is based on the exponential law proposed by Keddam et al. [32] which estimates the time constants of the nucleation and growth of the oxide layer. Therefore, it is necessary to have a complete record of the fall transient in order to determine precisely the time constants of the initiation and the growth of the oxide film. For the latency periods lower than 2 seconds, only the kinetic of the oxide film nucleation can be determined. For the latency periods higher than 2 seconds, the two times constants can be precisely defined, however the latency periods of 5 s do not increase the precision of the calculation. Therefore, this time allows clear observation of the current transient fall during the surface repassivation, as shown in Figure 9. The friction coefficients were evaluated based on the normal and tangential loads determined in the linear regime of sliding (calculation for cycles up to 150). The contact features of the ball-on-plane configuration were calculated based on Hertz assumptions for the two materials. Table 1 shows almost the same behavior for the two microstructures in terms of Hertz contact pressure and shear stresses. After the tribocorrosion tests, the pin curvature was controlled and only a change in 2 % was detected. In acidic solution, this corresponds to a limited wear of the corundum whereas in neutral and mostly in basic solution it corresponds to a material transfer from the

metal to pin. However, the wear on the pin can be considered as negligible in a first approximation regarding the wear measured on the AISI430-F and the AISI430-FM.

Table 1. Material properties and results of calculations based on Hertz assumptions.

Material	Young Modulus (GPa)	Poisson Coefficient	Hertz contact stress (MPa)	Shear Stress (MPa)	Shear stress position (µm)
AISI430-F	211	0.3	405	130	52
AISI430-FM	190	0.3	390	125	52

After tribocorrosion tests, wear volumes were determined from the methodology of Qu et al. [33], based on cross-sectional line measurements by ex situ contact profilometry (Somicronic, Surfascan 2D). Worn surfaces were examined using a field-emission scanning electron microscope (FE-SEM, Supra 55VP, Zeiss) in order to identify the wear mechanism. Microstructural analyses were completed by focused ion beam cross-section observations (FIB, NVision 40, Zeiss) to assess the subsurface modifications induced by the interaction between sliding and oxide film reformation [26].

Regarding the corundum pins, their curvatures after sliding were compared to their initial curvature. The results showed a slight increase of the curvature radius, mainly at higher potentials. Since no aluminum peak was detected on the wear tracks (by SEM-EDX analysis), this change was not attributed to the pin wear but to a metallic matter transfer from the stainless steel to the pin (EDS measurement detected iron, chromium and oxygen on the pin surface) that fills the pin roughness and helps in the formation of an adhesive compacted layer.

2.4 Electrochemical setup and parameters

Electrochemical experiments were performed using a three-electrode tribo-cell connected to a REF600 potentiostat (Gamry). The working electrodes were composed of stainless steel discs (10.2 cm^2 surface exposed to the electrolyte). A 16.0 cm^2 graphite disc was selected as the counter electrode and was

mounted above the working electrode (1 cm) to ensure uniform current line distribution during the experiments [34]. All potentials were applied versus a mercury sulphate electrode (E_{MSE} = +0.65 V/SHE). An aerated solution of 0.02 M H_2SO_4 (pH 1.4) was selected to avoid pitting corrosion. The experiments were performed at room temperature and in a stagnant solution.

Before each electrochemical measurement, a cathodic pretreatment was applied at -1.050 V/MSE for 30 min in order to significantly increase the measurement reproducibility [35] [1]. The passivation ability of the two stainless steels were determined from polarization curves recorded from -1.100 to +0.300 V/MSE at a scan rate of 0.5 mV/s. Electrochemical impedance spectroscopy measurements (EIS) were performed at different applied anodic potentials to qualitatively compare the passive film resistance. Selected potentials were applied for 1 hour after the surface pretreatment in order to reach current stability. The impedance diagrams were obtained over a frequency range of 10 kHz to 0.1 Hz with an amplitude of 5 mV_{rms} and 10 points per decade. Polarization curves and EIS measurements were not recorded during tribocorrosion tests, since the sliding frequency is not compatible with the acquisition frequency of EIS and the polarization scan rate [36]. Tribocorrosion tests were carried out at two different anodic potentials: -0.71 V/MSE and -0.05 V/MSE. Their selections are discussed in the results section. During sliding, current fluctuations were recorded at a frequency of 200 Hz.

3. Results and discussions

3.1 Microstructures and hardness descriptions

AISI430-F exhibits a globular microstructure with grain sizes in the range of 10 µm to 100 µm (Figure 2a). Micrographs also show chromium carbides heterogeneously distributed in the material. No signs of a chromium-depleted area surrounding the chromium carbides or at grain boundaries were detected by the Strauss test (ASTM A763-Practice 2). After the heat treatment, a dual phase microstructure was obtained with a ferrite matrix (grain sizes in the same range as AISI430-F) and martensite islands homogenously dispersed in the volume (Figure 2b). An image analysis (ImageJ software on Figure 2b) gives a martensite fraction of 25-30 %. Figure 2c shows that the solubilization of chromium carbides

during thermal treatment is partial, as some particles remain in the ferrite matrix. One consequence of the heat treatment was the generation of a balance difference of chromium between the two phases. Thus, Cr/Fe ratio is at approximately 21 at.% in ferrite and 20 at.% in martensite.

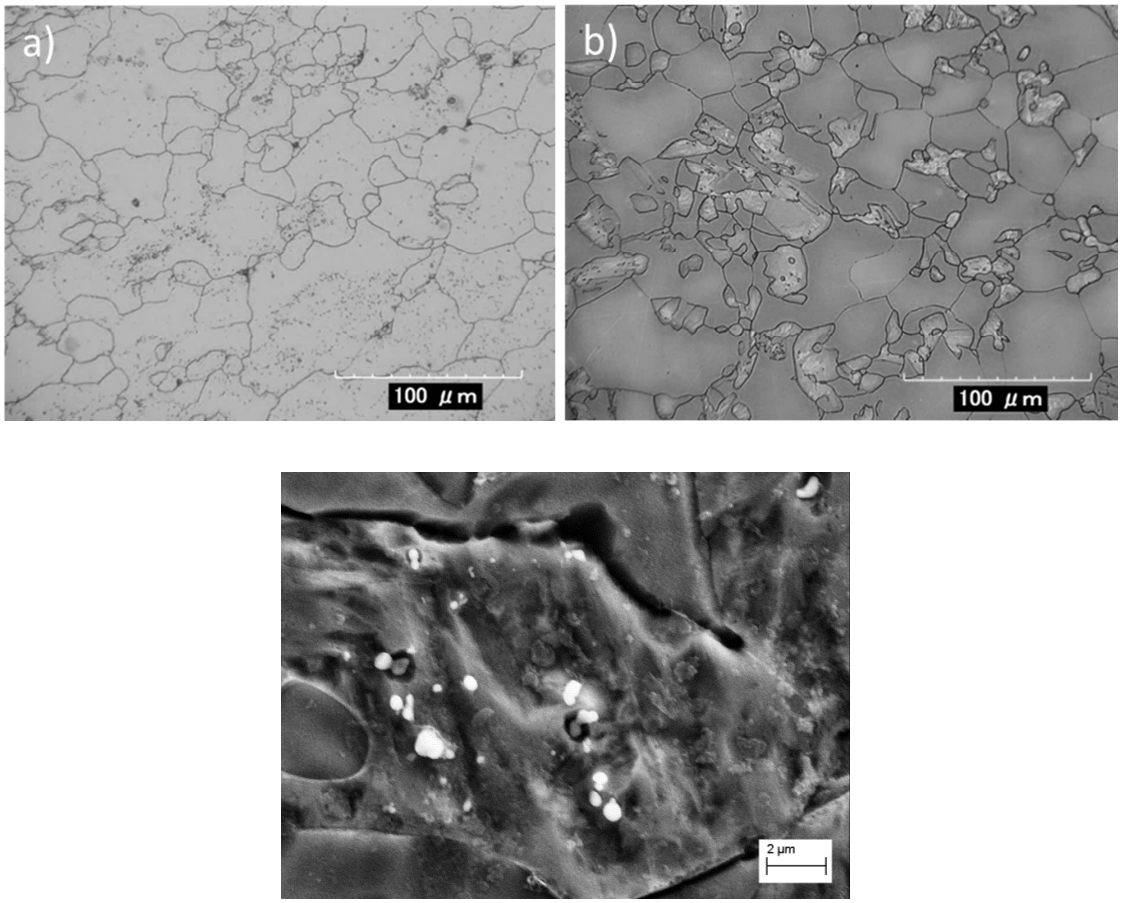

Figure 2. Optical observations after electrochemical etching of a) AISI430-F and b) AISI430-FM microstructures. c) SEM surface observation on AISI430-FM after chemical etching; white particles are chromium carbides (SEM-EDS).

In tribology, the wear rate is usually expressed by Archard's law, which is a function of the normal load and the hardness of the softer material in the contact. Since the normal load is fixed for all experiments, only the hardness of AISI430-F and AISI430-FM have to be evaluated. Microscopic hardness tests were thus performed on polished surfaces before the tribocorrosion experiments. An average value of 1.5 GPa was found for AISI430-F, whereas the hardness increased to 2.2 GPa for AISI430-FM. From nanohardness tests (Figure 3), the ferrite matrix in the dual phase exhibits a

hardness approximately 1 GPa higher than in AISI430-F. Thus, the enhancement detected for AISI430-FM stems from the greater hardness of the martensite and its reinforcement effect on the ferrite matrix [37]. In addition to the hardness, the corrosion behavior of the materials has to be considered since the passive film play a role in the wear resistance of the material [17].

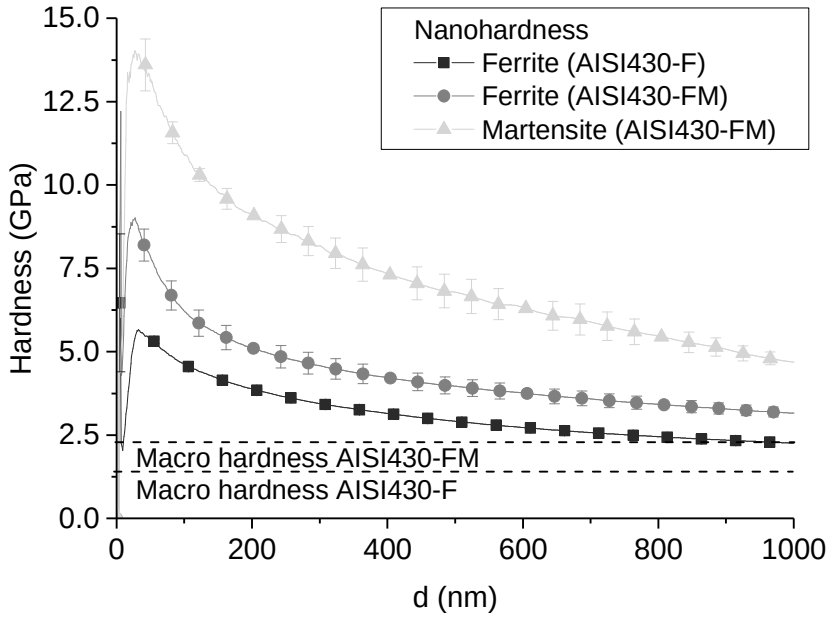

Figure 3. Hardness variation with the indentation penetration depth in ferrite (AISI430-F) and ferrite or martensite (AISI430FM) on polished surfaces before tribocorrosion. Scale bars are also reported on each curve; scale bars on ferrite (AISI430-F) are not visible at this scale but correspond to ± 0.02 GPa.

3.2. Corrosion behavior of two materials and potentials selection for tribocorrosion

Corrosion behaviors are described from polarization curves and impedance spectroscopy measurements recorded after a cathodic pretreatment at -1.05 V/MSE for 30 minutes. Figure 4a shows the potentiodynamic curves plotted from the cathodic to anodic domain for both stainless steels. In the cathodic domain (potentials lower than -0.95 V/MSE), currents are limited by charge transfer reactions such as the proton reduction usually encountered in acidic solutions. In the anodic region (potentials above -0.92 V/MSE), an active-passive peak is observed between -0.95 V/MSE and -0.73 V/MSE and linked to the metal dissolution (Cr^{2+} and Fe^{2+}) [38]. Since pH is higher than the depassivation pH,

materials passivate once a passive plateau (1 to 10 µA/cm²) is reached at higher potentials. Note that the current density is slightly higher for the dual phase microstructure, suggesting that the passive film requires more dissolution to remain at the steady state. In the case of the dual phase microstructure, the chromium distribution between the martensite and the ferrite generate a difference in term of film stability, such as a local galvanic coupling which acts negatively on the passivation. Therefore, more energy is required to keep the material at the passive steady state. On the passive plateau, the current density decreases from -0.71 V/MSE to -0.05 V/MSE for both materials, which indicates a reinforcement of the passive properties of the oxide layer with the potential. When impedance spectroscopy measurements are conducted at these two boundary potentials, Nyquist diagrams show an expansion of the pseudo-capacitive loops with the anodic potential (Figure 4b). From a qualitative viewpoint, this indicates a corrosion resistance enhancement with the maturation and thickening of the passive film at higher anodic potentials [19]. As previously observed on polarization curves, the pseudo-capacitive loop of AISI430-FM is lower than that of AISI430-F at a given potential. Usually, this corrosion resistance is ascribed to the effect of an alloying element. Since the chemical composition of the two materials are identical, it is attributed to the concentration difference of chromium in the ferrite and the martensite phases. Indeed, Jang et al. [39] demonstrated that even if a ferrite-martensite stainless steel tends to passivate, a galvanic coupling is established between the ferrite (cathodic site) and the martensite (anodic site). As a consequence of the galvanic coupling, the passive currents increase on polarization curves and the pseudo-capacitive loops decrease for AISI430-FM compared to AISI430-F.

As mentioned before, the chemical composition and the thickness of the oxide layer evolve with the applied potential in the passive domain. For Haupt and Strehblow [38] and Tanaka et al. [40], the metallurgy of the passive film changes from a Cr_2O_3 oxide layer at low anodic potentials to a compact Fe_2O_3/Cr_2O_3 layer at higher anodic potentials. When the applied potential reaches the transpassive region, the gradual increase of the current density is attributed to the field-assisted dissolution of Fe_2O_3. To compare the tribocorrosion behavior of the two materials, two potentials were selected in the passive domain. Note that similar potentials were chosen since the polarization curves for both

materials follow the same trend (Figure 4a). The first potential is fixed to -0.71 V/MSE in order to promote a surface repassivation by low stable Cr_2O_3 film, and the second is set at -0.05 V/MSE, where a compact Fe_2O_3/Cr_2O_3 layer exists on the surface.

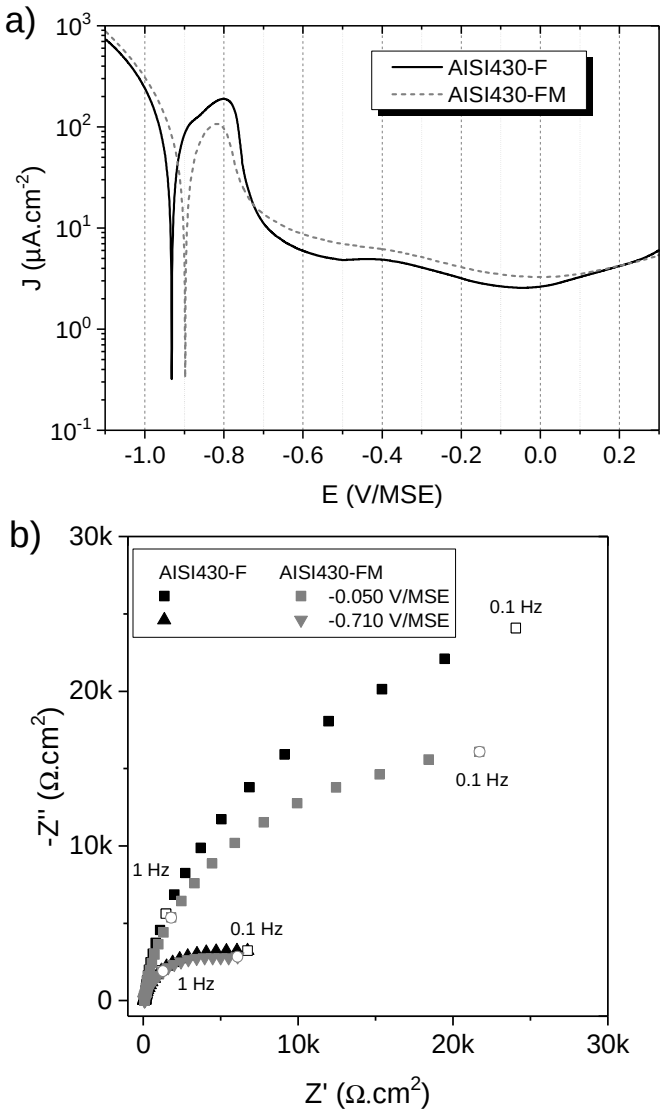

Figure 4. Electrochemical behavior of two stainless steels in an acidic solution described by a) polarization curves (scan rate of 0.5 mV/s) and b) electrochemical impedance measurements (Nyquist diagrams) recorded at -0.71 V/MSE and -0.05 V/MSE.

3.3. AISI430-F and AISI430-FM tribocorrosion behaviors

Tribocorrosion tests were performed at -0.71 V/MSE and -0.05 V/MSE under reciprocation in a solution with pH = 1.4. Currents flowing to the wear tracks are recorded according to a classical three electrode cell, and their variations are plotted in Figure 5b and Figure 5c. Irrespective of the applied potential, sliding activates the surface reactivity, which leads to large current fluctuations consisting of a finite sum of transients, as described later.

Figure 5a reports the wear rate as a function of the applied potential for the two stainless steels. The wear rates are in the range of 1.5 $x10^{-4}$ $mm^3.N^{-1}.m^{-1}$to 2.0 $x10^{-4}$ $mm^3.N^{-1}.m^{-1}$, with higher values for AISI430-F regardless of the potential. Even if the corrosion resistance of the dual phase is slightly lower than that of AISI430-F, the wear resistance remains controlled by the material hardness, which is positively affected by the martensite islands in the ferrite matrix for AISI430-FM [15]. Figure 5a also shows a slight increase of wear with the applied potential for both materials. This rise in wear is in line with the detrimental effects of a thicker and mature oxide layer, as often reported in the literature [41]. For a reciprocating motion with a significant latency period, the corrosion wear cannot be estimated from the average current recorded during the sliding because of their large fluctuations (Figure 5b and Figure 5c). Therefore, each transient of current has to be divided into two periods of time. The first one refers to the sharp increase of the current during the sliding whereas the second one refers to the decrease of the current induced by the repassivation of the surface. The current increase versus time corresponds to the electrical charge involved in the corrosion wear. This latter is calculated for each transient with the faraday's law where the equivalent molar weight of the metal is equal to 55.2 g/mol and the number of electrons exchanged is equal to 2.17 when only chromium and iron cations are considered [18]. In the literature, the mechanical wear is often estimated from sliding tests performed in the cathodic domain. It is worth noticing that either the contribution of the anodic reaction close to the OCP or the contribution of hydrogen charging for cathodic potential affect the mechanical wear determination [42], [43]. Therefore, the total wear volume is the sum of the mechanical wear and the corrosion wear where the synergistic terms of the wear accelerated corrosion and the corrosion accelerated wear are included in the corrosion wear and mechanical wear, respectively. Table 2 shows for each microstructure, the total wear volume as well as the corrosion

wear volume and the mechanical wear volume. Regardless the microstructure, the corrosion wear depends on the applied potential: higher the potential, stronger the corrosion wear will be. The mechanical wear decreases with the applied potential emphasizing the contribution of the corrosion damage at higher potential. Therefore, the chromium balance between the ferrite and the martensite in the dual phase material has no effect during the depassivation rate and the depassivation is not controlled by the microstructure. It can be noticed that the contribution of the mechanical wear in the total wear is slightly higher in the case of the AISI430-FM even if the wear resistance is improved by the dual phase microstructure. Irrespective of the microstructure and the potential, the mechanical wear is the dominant mechanism of degradation is in this work.

Table 2. Total wear volumes, mechanical wear volumes and corrosion wear volumes on AISI430-F and AISI430-FM after sliding at -0.71 V/MSE and -0.05 V/MSE.

Sample	Potential (V/MSE)	Total wear ($.10^{-3}$ mm^3)	Mechanical wear ($.10^{-3}$ mm^3)	Corrosion wear ($.10^{-3}$ mm^3)
AISI430-F	-0.71	36 ±3	33.7	2.3 ±0.5
	-0.05	38 ±3	29.2	8.8 ±0.5
AISI430-FM	-0.71	32 ±3	29.7	2.3 ±0.5
	-0.05	34 ±2	25.2	8.8 ±0.5

Figure 5a reports the average friction coefficient determined in the linear regime of wear for each test. No significant effect can be observed between the two microstructures and the two applied potentials. This can be attributed to the 10 N load applied during the sliding that not allowed to characterize a change in the surface condition.

At the beginning of sliding, sharp contacts promote a strong current increase as shown in Figure 5b and Figure 5c. At -0.71 V/MSE, the maximum current reaches approximately 5 $x10^{-4}$ A and is near 1.5 $x10^{-3}$ A at -0.05 V/MSE. Therefore, a higher overpotential enhances the surface dissolution in absence of a passive film (e.g., sliding period). Note that the current varies linearly with time after 1800 s and 7200 s at -0.71 V/MSE (Figure 5b) and -0.05 V/MSE (Figure 5c), respectively. This is due to the evolution of the wear tracks surface and the surface reactivity that depends on electrochemical and metallurgical parameters. At -0.71 V/MSE, the corrosion wear corresponds to 6% and 7% of the total

wear for the AISI430-F and AISI430-FM, respectively. At -0.05 V/MSE, the contribution of the corrosion wear in the total wear increases up to 23 % for AISI430-F and 26% for AISI430-FM. At the lowest potential (i.e., -0.71 V/MSE) the contribution of the corrosion wear is weak compared to the mechanical wear. Therefore, the evolution of the current with the time of sliding mainly depends on the mechanical wear and the hardness of the material (higher resistance for AISI430-FM). At -0.05 V/MSE, the contribution of the corrosion wear becomes less negligible, the wear resistance of the material is then controlled by its mechanical property, its microstructures and the passive film. On the one hand, a higher potential promotes a stronger passive film, enhances the contribution of the corrosion wear and increases the wear. On the other hand, the dual phase microstructure increases the hardness of the material and limits the wear.

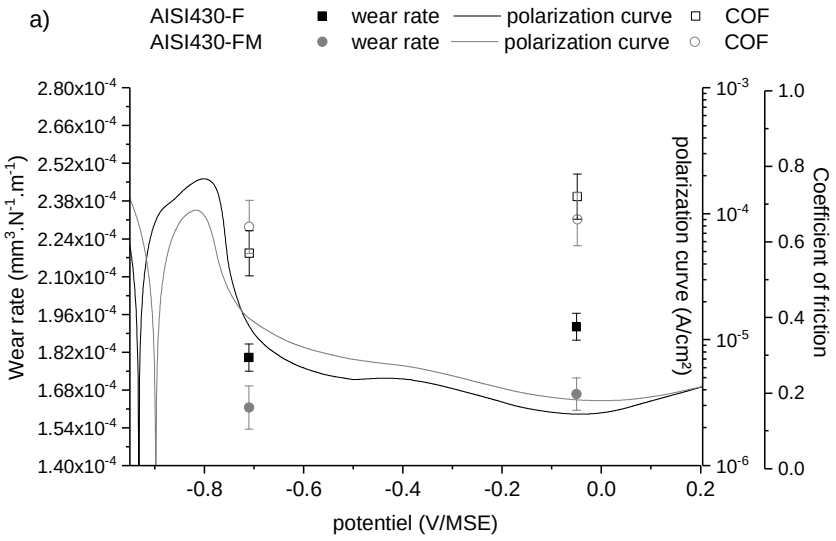
a)
AISI430-F
AISI430-FM
wear rate
polarization curve
COF
wear rate
polarization curve
COF
Wear rate (mm³.N⁻¹.m⁻¹)
polarization curve (A/cm²)
Coefficient of friction
potentiel (V/MSE)

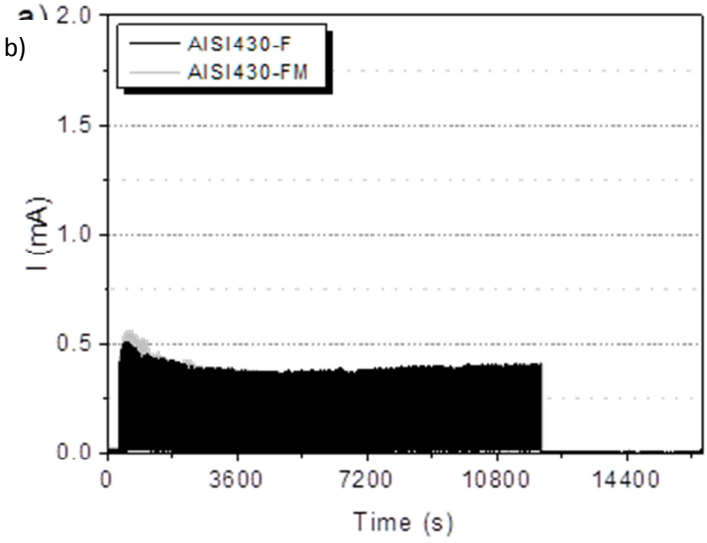
b)
AISI430-F
AISI430-FM
I (mA)
Time (s)

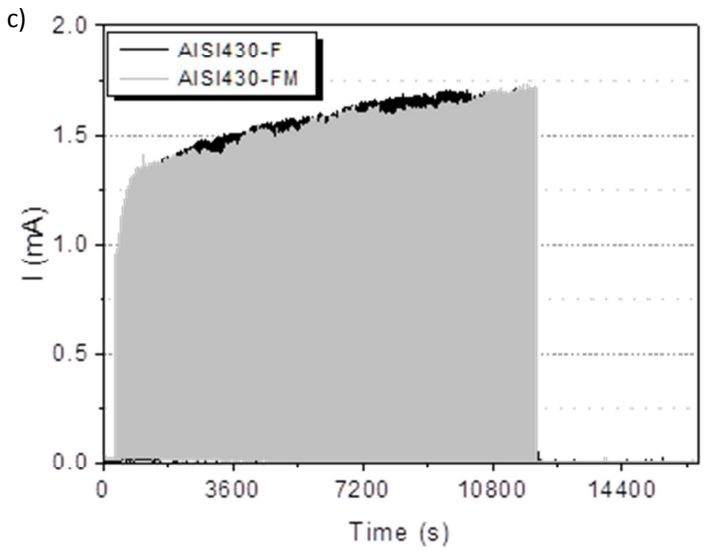

Figure 5. a) Tribocorrosion results expressed in terms of wear rate (filled symbols) and coefficient of friction (COF, open symbols) reported as a function of the applied potential for AISI430-F and AISI430-FM. Typical polarization curves in the anodic range are also reported. Current variations during tribocorrosion at b) -0.71 V/MSE and c) -0.05 V/MSE for both materials.

3.4. Worn surfaces observations

After tribocorrosion tests, worn surfaces were observed by SEM-EDS to identify the wear mechanism. On micrographs shown in Figure 6, grooves parallel to the sliding direction suggest an abrasive wear regardless of the material and potential. This is more pronounced for ASI430-F at -0.71 V/MSE (Figure 6a). For AISI430-FM (Figure 6b), microstructural decohesion is randomly detected as flakes in the same order of magnitude of the martensite islands. For sliding tests at -0.05 V/MSE, surfaces are more plastically deformed. Figure 6c and Figure 6d show an adhesive wear with surface plowing due to the oxide layer deformation for ASI430-F and AISI430-FM, respectively [38].

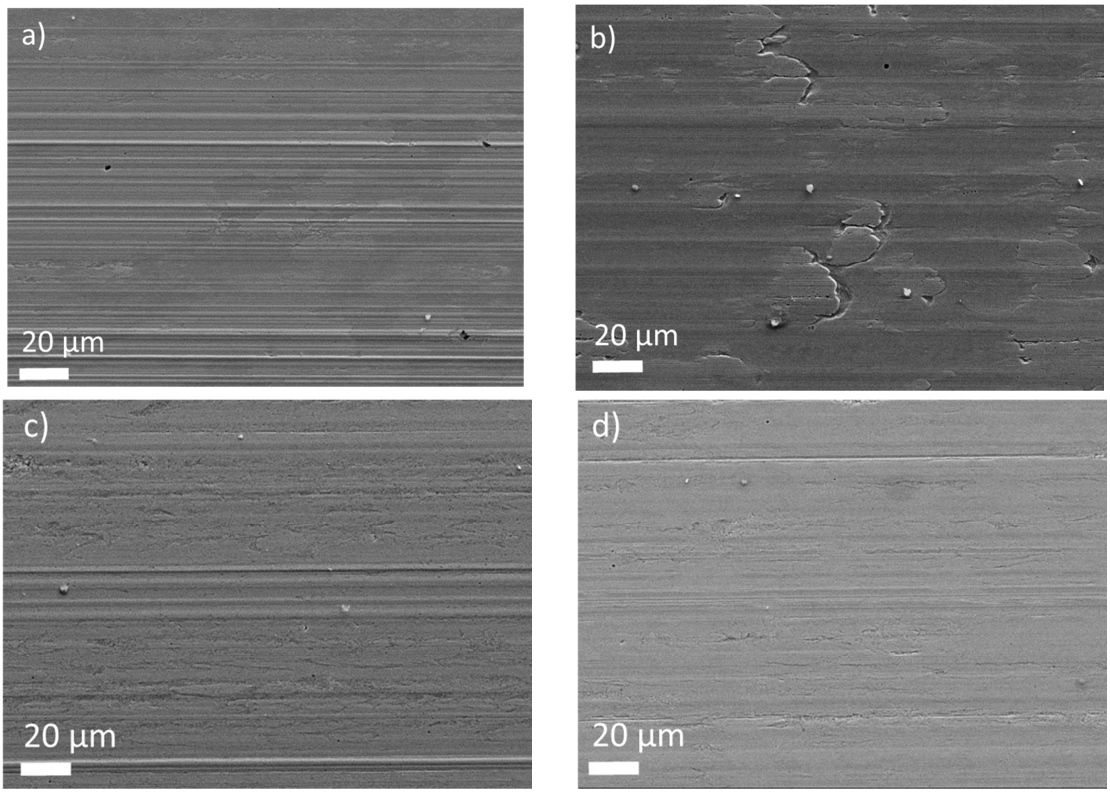

Figure 6. SEM images of worn surfaces after 1000 cycles of sliding at -0.71 V/MSE for a) AISI430 and b) AISI 430-FM and at -0.05 V/MSE for c) AISI430 and d) AISI 430-FM.

3.5. FIB-SEM cross-sections observations of the wear tracks

Cross-section observations perpendicular to the direction of sliding were obtained to evaluate the microstructural damage underneath the wear track. Note that the damages reported below are the consequence of the sum of unitary interactions between the surface reactivity and the mechanical load.

At -0.71 V/MSE, Figure 7a shows a grain refined layer homogenously distributed in the plane direction to a 2-3 µm depth for ASI430-F. At higher magnification, FIB-SEM images show a well-defined subsurface microstructure with nanometric grains ending at the edges of the etched layer (Figure 7b). Since abrasive wear was defined in Figure 6, these grooves come from the pin indent in the stainless steel but also from the grains' dissolution that takes place during surface dissolution influenced by the crystallographic orientations [44]. At -0.05 V/MSE, the grain refined layer depth increases until reaching 4 µm to 6 µm (Figure 7c). Here, grains are no longer parallel to the sample surface and exhibit preferential orientations related to the presence of defects on the worn surface.

Since the mechanical properties of the sliding are kept constant, the grain refined layer thickens under the influence of the passive film. Figure 7d shows that oxides or third bodies embed in grooves at -0.05 V/MSE, reducing the waviness of the surface. At higher magnification, they present a flake structure that favors surface plowing (Figure 7) and easily transfer to the pin surface. An adhesive surface is then formed, which consequently increases the friction coefficient as already mentioned at Figure 5a. Note that chromium carbides might also be incorporated into the third layer; however, none have been detected in the oxide layer or at the surface irrespective of the potential. These cross-sectional analyses also show that no cracks generate and propagate into the material volume.

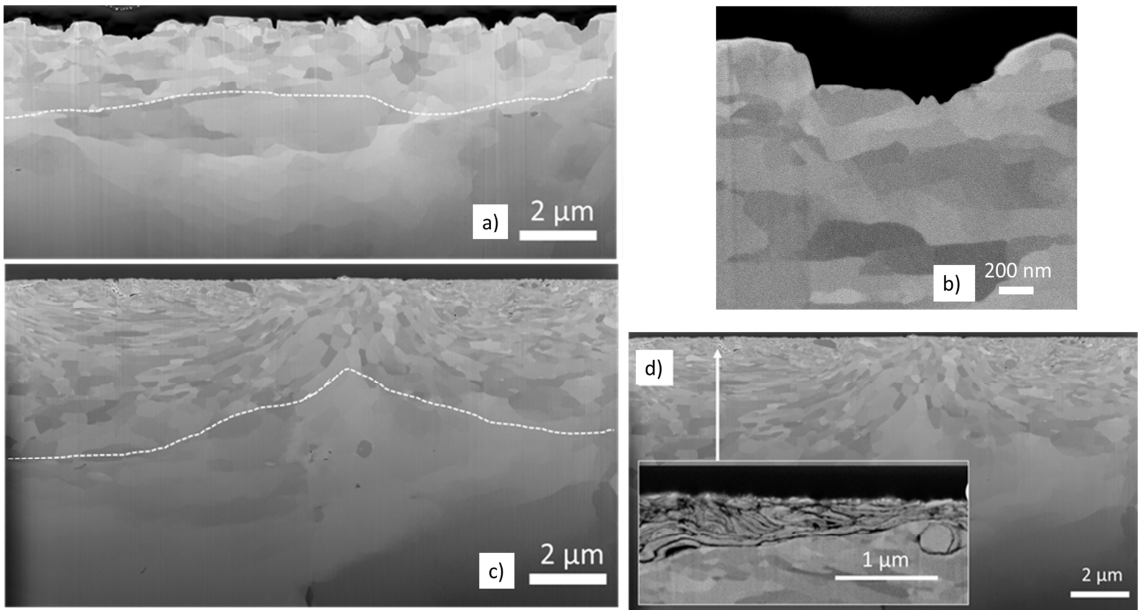

Figure 7. FIB-SEM analysis on ASI430F at -0.71 V/MSE a) large scale observation and b) detail underneath the surface. c) Grain refined microstructure at -0.05 V/MSE and d) detail of the oxide layer embedding. White dash lines highlight the TTL, including the tribolayer and the deformed region. Images taken in the perpendicular direction of sliding

AISI430-FM presents the same trend that AISI430-F. Thus, a dynamic recrystallization takes place in the first micrometers underneath the surface at -0.71 V/MSE (Figure 8a). However, grain refinement is located only in the ferrite. Some highly deformed zones are also observed in martensite, but they coincide with surface defects such as those observed in Figure 6b. Because of the martensite reinforcement, ferrite refined grains present a preferential orientation in the perpendicular plane of the

worn surface. Moreover, the refined microstructure is less well-defined than that of AISI430-F because of constraint induced by the martensite islands that limits the deformation direction and increases stress in the ferrite. At -0.05 V/MSE, the grain refinement layer thickens until reaching 6 µm to 8 µm, which is slightly higher than for AISI430-F (Figure 8c), with still a dynamic recrystallization in the ferrite. Oxide debris are also imbedded into the surface roughness. Since the lamellar structures, they detach from the worn surface. Since no material transfer is observed on the counter parts, the increase of wear is attributed to the enhancement of the corrosive wear as shown before and a change in the passive film composition and thickness. In comparison to AISI430-F, not only the passive film but also martensite islands interact with the pin during sliding. The latter offer hard points during the pin motion, which could reduce the adhesive contribution of the oxide layer [45]. However, these changes in the surface conditions cannot be detected by the COF since the normal load selected in this work is too high.

For AISI430-FM, no cracks propagate into the material volume, confirming the beneficial effect of percolated martensite islands in the ferrite.

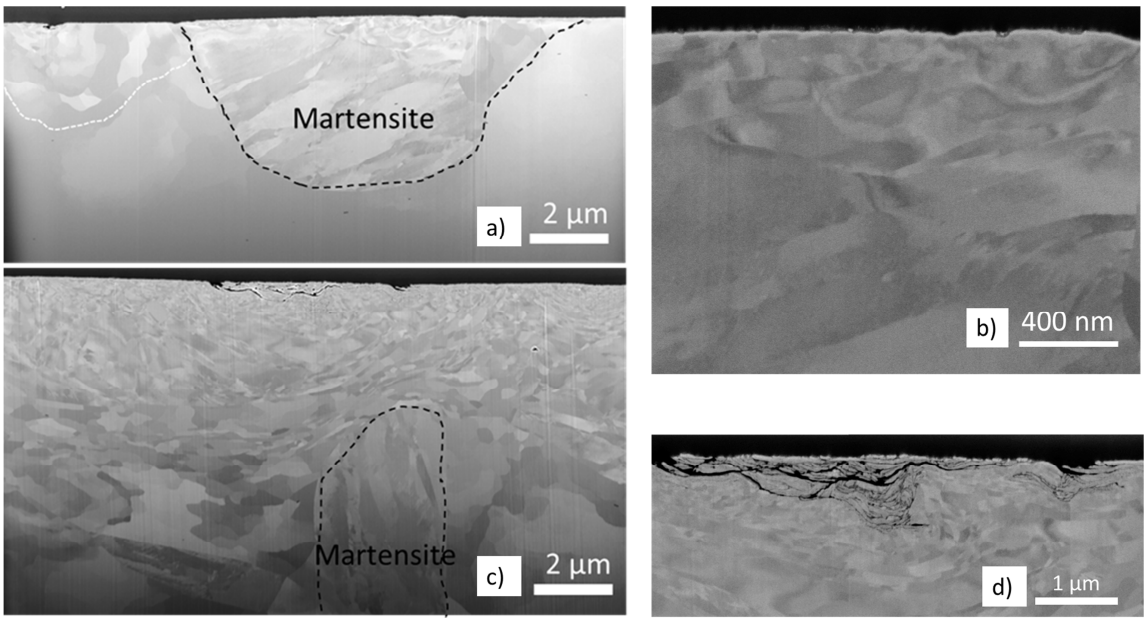

Figure 8. FIB-SEM analysis on ASI430FM at -0.71 V/MSE a) large scale observation and b) detail underneath the surface. c) Grain refined microstructure at 0.05 V/MSE and d) detail of the oxide layer embedding. Images taken in the perpendicular direction of sliding

3.6. Repassivation kinetics quantification

Figure 9a and Figure 9b display representative current transient rises in the linear regime of wear for AISI430-F and AISI430-FM, respectively. The absence of differences in terms of maximum current reached indicate that the two materials behave in similar manners because of their shared chemical composition. Therefore, the strongest effect observed in Figure 9a and Figure 9b comes from the applied potential, as has been already described at Figure 5.

Figure 9c and Figure 9d present falling current transients recorded during the latency period in the linear regime of wear of AISI430-F and AISI430-FM, respectively. If it is easily noticed that the transient becomes steeper at higher anodic potential and this increases the curve slope, it is more difficult to distinguish the influence of the microstructure on the repassivation rate. To achieve that, experimental curves have to be fitted by models that provide quantitative information on the repassivation kinetics.

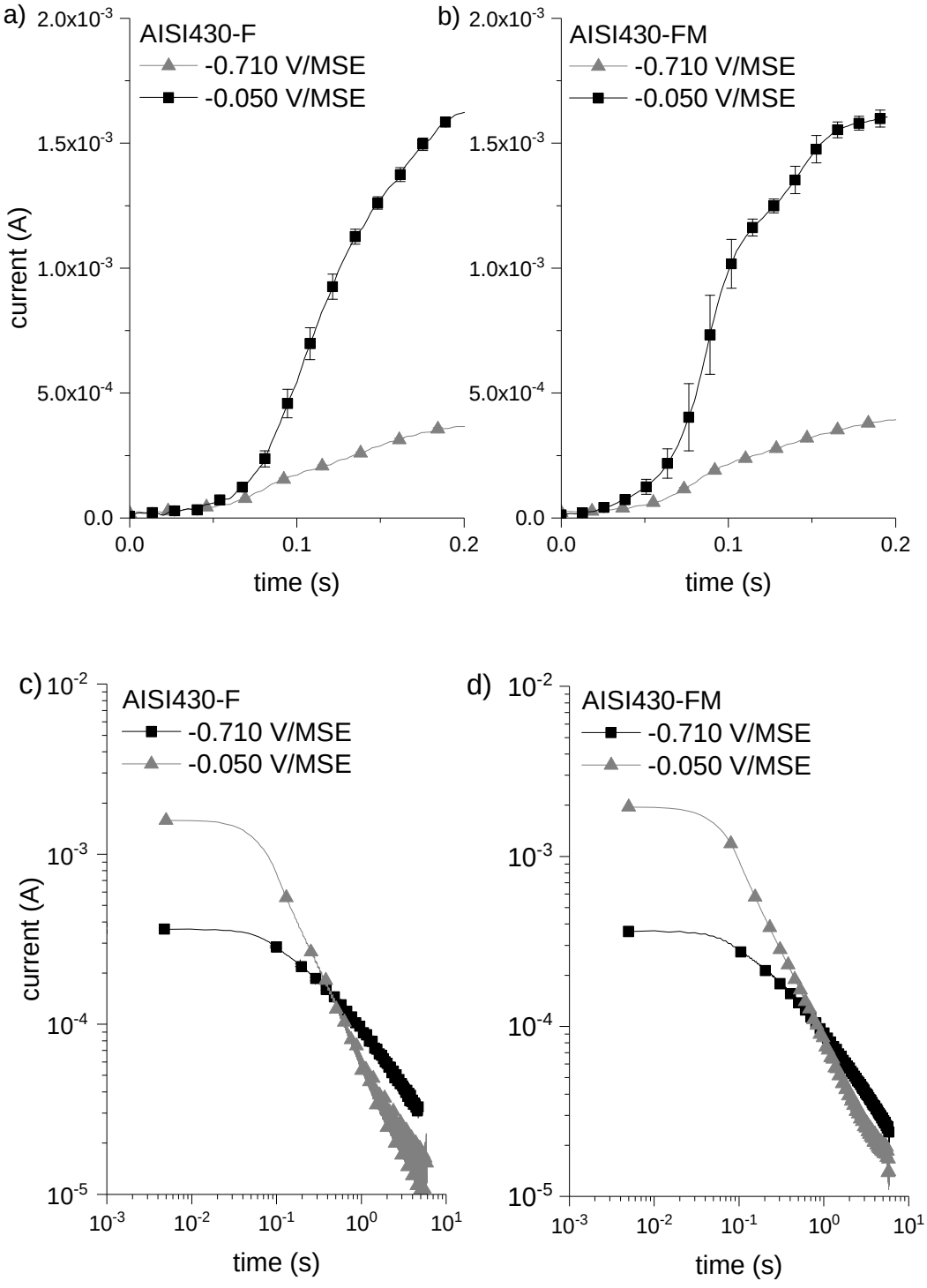

Figure 9. Current transients rise during sliding on a) AISI430-F and b) AISI430-FM. Current fall during the idle periods for c) AISI430-F and d) AISI430-FM.

In the literature, Jemmely et al. [18] and Olsson and Stemp [46] proposed numerical models to simulate the overall current transients during tribocorrosion. These are based on the High Field model and the Interface Field model, respectively. For the High Field model [47], [48], the thickening mechanism is controlled by cationic emission at the metal/film interface, whereas the limiting step in the Interface Field model is supposed to be the formation of O^{2-} by water splitting at the film/solution interface [49]. Among other descriptors, the oxide film thickness, charge transfer coefficients, and ohmic drop can be evaluated through these models. While their approach works well for short stroke lengths, no conclusive results were obtained here since the depassivation distance is larger. Another approach consists of a temporal analysis of the falling current transient that can be applied independently to experimental conditions. For Keddam et al. [32] and Okorie et al. [50], the earlier step of the repassivation consists of a reaction between metallic ionic species (originating from the sliding) with oxygen from water molecules to form $M(OH)_x$ adsorbates and later a 2D oxide layer by deprotonation of hydrated species [51], [52]. When the 2D clusters merge together, oxide thickening starts according to Okamoto's model [53]. This two-step mechanism can be written according Equation 1, where the first step of the repassivation (2D) is characterized by a high current amplitude (A_{2D}) and a short time constant (τ_{2D}), whereas the 3D structuration of the passive film is characterized by lower A_{3D} and τ_{3D} parameters [32], [54]. Note that the double layer rebuild and the oxide aging are not considered since they occur in the first milliseconds of the transient or in the range of hours, respectively [34], [55]. In Equation 1, a limiting current (i_0) was also introduced to account for the steady state current of the passive film at the end of the idle period.

$$i = i_0 + A_{2D}.\exp\left(-{}^{t}/_{\tau_{2D}}\right) + A_{3D}.\exp\left(-{}^{t}/_{\tau_{3D}}\right) \qquad \text{Equation 1}$$

Figure 10 shows curves fitted at -0.71 V/MSE and -0.05 V/MSE for falling current transients on AISI430-F. Since good accuracy is obtained between fitted and experimental curves, the time constants τ_{2D} and τ_{3D} can be considered to describe the worn surface repassivation rate.

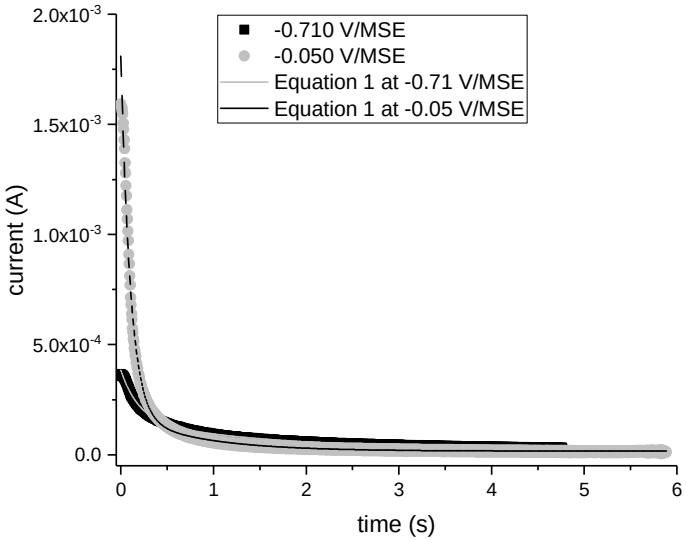

Figure 10. Example of current transient fitting with Equation 1 at -0.71 V/MSE and -0.05 V/MSE on AISI430-F. Note that currents are extracted in the linear regime wear (time higher than 6 x10^3 seconds in Figure 5a)

Table 2 reports the amplitude and time constant values calculated from Equation 1 according to the applied potential and the microstructure. Regardless of material, i_0 is lower at -0.05 V/MSE than at -0.71 V/MSE, which confirms that the oxide film resistance is higher at -0.05 V/MSE, even if surface is mechanically deformed.

Table 2. Average values from cycles ranged from 500 to 1000, for the four parameters of Equation 1. The adjusted R-square is > 0.995.

			2D mechanism		3D mechanism	
Samples	Potential (V/MSE)	i_0 (× 10^{-6} A) (± 5× 10^{-6})	τ_{2D} (s) (± 0.04)	Amplitude A_{2D} (× 10^{-4} A) (± 0.5× 10^{-4})	τ_{3D} (s) (± 0.04)	Amplitude A_{3D} (× 10^{-4} A) (± 0.5× 10^{-4})
AISI430-F	-0.710	31	0.15	1.7	1.00	1.5
	-0.050	20	0.06	20.0	0.50	3.5
AISI430-FM	-0.710	32	0.20	2.5	1.40	1.3
	-0.050	17	0.10	17.5	0.80	1.8

For a given microstructure, the potential rise promotes higher current amplitude values (A_{2D} and A_{3D}) and a reduction of the times constants τ_{2D} and τ_{3D}. The current contribution of the 2D is in the range of 2 x10^{-4} A at -0.71 V/MSE and reaches 20 x10^{-4} A at -0.05 V/MSE. The A_{2D} dependence on the

potential is consistent with the time-current relation for instantaneous nucleation and growth given by Okorie and Nowak [50], who linked the current amplitude of a transient to the charge involved in the monolayer formation and a constant depending on potential. For A_{3D}, the effect of the potential is less marked since the oxide film thickening is mostly limited by diffusion-migration rather than charge transfer.

For the repassivation constants, τ_{2D} values (0.06 - 0.2 seconds) coincide with a charge transfer limitation linked to the germination of the oxide film, whereas τ_{3D} values (0.5 – 1.4 seconds) are related to a diffusion/migration-controlled regime usually occurring during the oxide thickening according to Strehblow [56]. Irrespective of the microstructure, a potential shift from -0.71 V/MSE to -0.05 V/MSE leads to lower τ_{2D} and τ_{3D}. The reduction of the time constants indicates that the oxide film rebuild is faster at higher overpotentials. Indeed, the precipitation of $M(OH)_x$ adsorbates in the iono-selective layer at the worn surface is facilitated by the concentration increase of Cr^{3+} and/or Fe^{3+} at -0.05 V/MSE (Figure 9a and Figure 9b), whereas the potential difference between the solution and the material aid the diffusion-migration mechanism during the oxide thickening [56]–[58]. Table 2 also reveals that the microstructure has an effect on the repassivation kinetics. Indeed, the time constants (τ_{2D}, τ_{3D}) exhibit slightly higher values for AISI-430FM than AISI430-F. This decrease in passivation ability for the dual phase microstructure can be related to the galvanic coupling between the ferrite and the martensite, which impedes the ability of the surface to become passive, as already observed on Figure 4a. Therefore, the quantification of the repassivation rate shows that anodic potential promotes the repassivation kinetics of the wear track whereas the coexistence of martensite and ferrite destabilize the formation of the passive layer. If the repassivation rates (Table 2) are compared to wear rates (Figure 5a), it can be noticed that the wear increases at higher oxide rebuild kinetics, confirming that the presence of the passive layer in the contact is detrimental for the material resistance [17]. However, the order of magnitude of variation of those parameters suggest that the oxide layer has a lower role on the material degradation than the pin contact and the stainless steel microstructure.

3.7. Influence of the repassivation kinetics on the sub-surface microstructures.

In tribocorrosion, wear resistance arises from a combination of external factors such as environmental conditions, mechanical properties of the contact surfaces, and internal factors depending on the material characteristics. Usually, those are related to the material chemistry, microstructure and electrochemical behavior in solution. In most of the cases, the wear resistance of passive alloys is driven by the hardness of the material as long as no cracks are generated that can propagate during sliding. To improve material hardness, the microstructure and chemical composition of alloys can be adjusted, or a specific heat treatment can be performed. Here, the general purpose of the heat treatment was to solubilize chromium carbide initially present in a commercial ferrite stainless steel (AISI430-F) in order to grow martensite islands in ferrite matrix (AISI430-FM). Macroscopic hardness measurements confirmed the beneficial effect of the martensite islands in the ferrite matrix (hardness increase of 0.7 GPa). Using nanohardness tests, this improvement was linked not only to the martensite properties but also an increase of the hardness in the ferrite by a matrix reinforcement effect. Consequently, a lower wear rate was obtained for the dual phase microstructure for sliding performed in the passive domain at -0.71 V/MSE and -0.05 V/MSE (Figure 5a).

Figure 5a has also shown that the wear rates increase with the applied potential for both materials. Note, however, that this trend is less marked for AISI430-FM. Surface observations highlighted that abrasive wear mostly occurred at the beginning of the passive plateau (i.e., tests at -0.71 V/MSE) whereas abrasive/adhesive wear took place at a higher passive potential (i.e., -0.05 V/MSE). This trend was linked to the oxide film properties. At -0.71 V/MSE, the oxide layer is mainly composed of Cr_2O_3, whereas an iron enrichment occurs at -0.05 V/MSE [38]. Since the hardness of the chromium oxide layer decreases with iron injection [38], [40], wear increases at -0.05 V/MSE due to the formation of an adhesive interface between the pin and sample, as observed for AISI430-F [59]. In the case of AISI430-FM, the wear increase is less marked due to the presence of martensite islands that limit the pin indents. Moreover, the oxide film mostly grows on the ferrite due to the galvanic coupling with the

martensite, which could reduce the quantity of oxide that participates in the adhesive layer between the worn surface and the pin [39].

FIB-SEM analysis shows the presence of a grain refined layer in which the thickness depends on the potentials and less on the range of the microstructure. From Beyglezimer [60], the grain division process is controlled by the pressure, temperature and the strain rate. If the strain rate and the temperature are assumed to be equivalent between all tests, only the pressure should be investigated. On the one hand, the pin load and pin motion generate dislocation in the material volume that is partially annihilated with the surface corrosion during sliding. On the other, the oxide film rebuild blocks the metal dissolution and the dislocation flow toward the surface. Therefore, a dynamic recrystallization by accumulation of plastic deformation initiates as function of the repassivation kinetics. During the pin latency period, the current fall analysis highlights that the anodic potential favors a faster kinetic of repassivation compared to the potential close to the active-passive region. Since the dislocation density underneath the surface increases, a thicker grain refinement takes place and consequently increases the surface strain hardening [61]. With the mechanical load applied, this grain refined layer could not act as a hard layer in the contact and promotes wear, in addition to the adhesive effect of the oxide layer in the contact [62]. Therefore, the main influence of the passive reformation concerns the sub-surface modifications in this work. To better characterize the role of the repassivation rate in wear, further experiments have to be performed at lower mechanical loads to decrease the contribution of the mechanical wear in the corrosion wear mechanism and enhance the effect of the oxide film in wear.

Conclusions

This paper evaluated the tribocorrosion resistance of a ferrite and ferrite martensite stainless steel for two applied potentials in the passive domain. The dual phase microstructure was obtained by thermal treatment of the ferrite stainless in order to maintain the chemical composition of the two materials. Tests were performed in an acidic solution at -0.71 V/MSE and -0.05 V/MSE. Those potentials

correspond to the beginning and end of the passive plateau for both samples. A reciprocating motion was used to monitor the surface reactivity under sliding and the current transients fall during the latency period. Surface and cross-section observations were performed, and numerical analysis was carried out on current transient falls to characterize the repassivation rate of the worn surface. From that, several results have been obtained and can be summarized as:

- Regardless of the potential, the dual phase microstructure presents a higher tribocorrosion resistance. This was attributed to the composite matrix effect induced by the presence of martensite islands in the ferrite matrix.
- Wear rate slightly increases at higher potentials whatever the microstructure. Since adhesion wear was detected on the worn surfaces, the damage enhancement was attributed to the nature of the passive film that deformed more easily due to an iron enrichment in the Cr_2O_3 layer. Note that the corrosion wear contribution also increases at higher anodic potential.
- On the one hand, the repassivation rate was not directly correlated to the wear resistance since the mechanical load was too high. On the other hand, it has been shown that the film reformation kinetics play a role on the dynamic recrystallization underneath the worn surface. A fast oxidation rate blocks the annihilation of dislocations by dissolution and promotes a larger grain refinement layer that is not able to support the mechanical load in this study.

Acknowledgments and conflict of interest statement

The authors are grateful to R. Di-Folco (MATEIS) and A. Gaugain (APERAM, Isbergue France) for providing the electrochemical cell and materials.

Bibliography

[1] T. W. Chenje, D. J. Simbi, et E. Navara, « Relationship between microstructure, hardness, impact toughness and wear performance of selected grinding media for mineral ore milling operations », *Materials & Design*, vol. 25, n° 1, p. 11‑18, févr. 2004.

[2] H. Holleck, « Material selection for hard coatings », *Journal of Vacuum Science & Technology A: Vacuum, Surfaces, and Films*, vol. 4, n° 6, p. 2661‑2669, nov. 1986.

[3] K. Sriram, R. Narasimhan, et S. K. Biswas, « A numerical fracture analysis of indentation into thin hard films on soft substrates », *Engineering Fracture Mechanics*, vol. 70, n° 10, p. 1323‑1338, juillet 2003.

[4] B. Basu, J. Vleugels, et O. Van Der Biest, « Microstructure–toughness–wear relationship of tetragonal zirconia ceramics », *Journal of the European Ceramic Society*, vol. 24, n° 7, p. 2031‑2040, juin 2004.

[5] S. Cao et S. Mischler, « Assessment of a recent tribocorrosion model for wear of metal-on-metal hip joints: Comparison between model predictions and simulator results », *Wear*, vol. 362–363, p. 170‑178, sept. 2016.

[6] J. F. Li *et al.*, « Uniform design method for optimization of process parameters of plasma sprayed TiN coatings », *Surface and Coatings Technology*, vol. 176, n° 1, p. 1‑13, nov. 2003.

[7] J. F. Archard, « Contact and Rubbing of Flat Surfaces », *Journal of Applied Physics*, vol. 24, n° 8, p. 981‑988, août 1953.

[8] J. F. Archard et W. Hirst, « The Wear of Metals under Unlubricated Conditions », *Proc. R. Soc. Lond. A*, vol. 236, n° 1206, p. 397‑410, août 1956.

[9] D. Landolt, S. Mischler, et M. Stemp, « Electrochemical methods in tribocorrosion: a critical appraisal », *Electrochimica Acta*, vol. 46, n° 24–25, p. 3913–3929, 2001.

[10] E. Huttunen-Saarivirta, L. Kilpi, T. J. Hakala, L. Carpen, et H. Ronkainen, « Tribocorrosion study of martensitic and austenitic stainless steels in 0.01 M NaCl solution », *Tribology International*, vol. 95, p. 358‑371, mars 2016.

[11] P. Lacombe, Éd., *Stainless steels*. Les Ulis: Les Ed. de Physique, 1993.

[12] B. H, « Increasing the wear resistance of stainless steels », *Materialwissenschaft und Werkstofftechnik*, vol. 38, n° 6, p. 464‑472, juin 2007.

[13] V. Vignal, N. Mary, P. Ponthiaux, et F. Wenger, « Influence of friction on the local mechanical and electrochemical behaviour of duplex stainless steels », *Wear*, vol. 261, n° 9, p. 947‑953, nov. 2006.

[14] M. Aksoy, M. B. Karamiş, et E. Evin, « An evaluation of the wear behaviour of a dual-phase low-carbon steel », *Wear*, vol. 193, n° 2, p. 248‑252, mai 1996.

[15] X. Xu, W. Xu, F. H. Ederveen, et S. van der Zwaag, « Design of low hardness abrasion resistant steels », *Wear*, vol. 301, n° 1–2, p. 89‑93, avril 2013.

[16] H. Saghafian et S. Kheirandish, « Correlating microstructural features with wear resistance of dual phase steel », *Materials Letters*, vol. 61, n° 14–15, p. 3059‑3063, juin 2007.

[17] S. Mischler, A. Spiegel, et D. Landolt, « The role of passive oxide films on the degradation of steel in tribocorrosion systems », *Wear*, vol. 225–229, Part 2, n° 0, p. 1078–1087, 1999.

[18] P. Jemmely, S. Mischler, et D. Landolt, « Electrochemical modeling of passivation phenomena in tribocorrosion », *Wear*, vol. 237, n° 1, p. 63–76, janv. 2000.

[19] I. Olefjord et L. Wegrelius, « Surface analysis of passive state », *Corrosion Science*, vol. 31, p. 89‑98, 1990.

[20] D. Landolt, S. Mischler, M. Stemp, et S. Barril, « Third body effects and material fluxes in tribocorrosion systems involving a sliding contact », *Wear*, vol. 256, n° 5, p. 517‑524, mars 2004.

[21] J. L. Tipper, P. J. Firkins, E. Ingham, J. Fisher, M. H. Stone, et R. Farrar, « Quantitative analysis of the wear and wear debris from low and high carbon content cobalt chrome alloys used in metal on metal total hip replacements », *Journal of Materials Science: Materials in Medicine*, vol. 10, n° 6, p. 353‑362, juin 1999.

[22] D. A. Rigney et W. A. Glaeser, « The significance of near surface microstructure in the wear process », *Wear*, vol. 46, n° 1, p. 241‑250, janv. 1978.
[23] R. W. Staehle, « Transient stability of passive films in aqueous solutions », *Corrosion Science*, vol. 49, n° 1, p. 7‑19, janv. 2007.
[24] A. Bidiville, M. Favero, P. Stadelmann, et S. Mischler, « Effect of surface chemistry on the mechanical response of metals in sliding tribocorrosion systems », *Wear*, vol. 263, n° 1–6, p. 207‑217, sept. 2007.
[25] M. Favero, P. Stadelmann, et S. Mischler, « Effect of the applied potential of the near surface microstructure of a 316L steel submitted to tribocorrosion in sulfuric acid », *J. Phys. D: Appl. Phys.*, vol. 39, n° 15, p. 3175, août 2006.
[26] J. Perret *et al.*, « EBSD, SEM and FIB characterisation of subsurface deformation during tribocorrosion of stainless steel in sulphuric acid », *Wear*, vol. 269, n° 5–6, p. 383–393, 2010.
[27] R. Büscher et A. Fischer, « The pathways of dynamic recrystallization in all-metal hip joints », *Wear*, vol. 259, n° 7–12, p. 887‑897, juillet 2005.
[28] M. A. Moore et R. M. Douthwaite, « Plastic deformation below worn surfaces », *MTA*, vol. 7, n° 12, p. 1833‑1839, déc. 1976.
[29] V. G. Efremenko, K. Shimizu, T. Noguchi, A. V. Efremenko, et Y. G. Chabak, « Impact–abrasive–corrosion wear of Fe-based alloys: Influence of microstructure and chemical composition upon wear resistance », *Wear*, vol. 305, n° 1–2, p. 155‑165, juillet 2013.
[30] M. Moine, N. Mary, B. Normand, L. Peguet, A. Gaugain, et H. N. Evin, « Tribo electrochemical behavior of ferrite and ferrite–martensite stainless steels in chloride and sulfate media », *Wear*, vol. 292–293, n° 0, p. 41‑48, juill. 2012.
[31] X. Li et B. Bhushan, « A review of nanoindentation continuous stiffness measurement technique and its applications », *Materials Characterization*, vol. 48, n° 1, p. 11‑36, février 2002.
[32] M. Keddam, P. Ponthiaux, et V. Vivier, « Tribo-electrochemical impedance: A new technique for mechanistic study in tribocorrosion », *Electrochimica Acta*, oct. 2013.
[33] J. Qu et J. J. Truhan, « An efficient method for accurately determining wear volumes of sliders with non-flat wear scars and compound curvatures », *Wear*, vol. 261, n° 7–8, p. 848–855, oct. 2006.
[34] A. Berradja, D. Déforge, R. P. Nogueira, P. Ponthiaux, F. Wenger, et J.-P. Celis, « An electrochemical noise study of tribocorrosion processes of AISI 304 L in Cl − and media », vol. 39, n° 15, p. 3184–3192, août 2006.
[35] J. Geringer, B. Normand, C. Alemany-Dumont, et R. Diemiaszonek, « Assessing the tribocorrosion behaviour of Cu and Al by electrochemical impedance spectroscopy », *Tribology International*, vol. 43, n° 11, p. 1991‑1999, nov. 2010.
[36] J. Geringer, J. Pellier, M. L. Taylor, et D. D. Macdonald, « Electrochemical Impedance Spectroscopy: Insights for fretting corrosion experiments », *Tribology International*, sept. 2013.
[37] M. Delince, P. Jacques, et T. Pardoen, « Separation of size-dependent strengthening contributions in fine-grained Dual Phase steels by nanoindentation », *Acta Materialia*, vol. 54, n° 12, p. 3395‑3404, juill. 2006.
[38] S. Haupt et H.-H. Strehblow, « A combined surface analytical and electrochemical study of the formation of passive layers on FeCr alloys in 0.5 M H2SO4 », *Corrosion Science*, vol. 37, n° 1, p. 43‑54, janv. 1995.
[39] J. W. Jang, I. Iwasaki, et J. J. Moore, « The Effect of Galvanic Interaction Between Martensite and Ferrite in Grinding Media Wear », *CORROSION*, vol. 45, n° 5, p. 402‑407, mai 1989.
[40] S. Tanaka, N. Hara, et K. Sugimoto, « Corrosion characteristics of Fe2O3‑Cr2O3 artificial passivation films under potentiostatic control », *Materials Science and Engineering: A*, vol. 198, n° 1–2, p. 63‑69, juillet 1995.
[41] L. Benea, P. Ponthiaux, F. Wenger, J. Galland, D. Hertz, et J. . Malo, « Tribocorrosion of stellite 6 in sulphuric acid medium: electrochemical behaviour and wear », *Wear*, vol. 256, n° 9–10, p. 948‑953, mai 2004.

[42] E. P. Georgiou *et al.*, « Effect of cathodic hydrogen charging on the wear behavior of 5754 Al alloy », *Wear*, vol. 390, n° Supplement C, p. 295‑301, nov. 2017.
[43] S. Akonko, D. Y. Li, et M. Ziomek-Moroz, « Effects of cathodic protection on corrosive wear of 304 stainless steel », *Tribol Lett*, vol. 18, n° 3, p. 405‑410, mars 2005.
[44] A. Sato, K. Kon, S. Tsujikawa, et Y. Hisamatsu, « Effect of Crystallographic Orientation on Dissolution Behavior of Stainless Steels Single Crystal », *Mater. Trans., JIM*, vol. 37, n° 4, p. 729‑732, 1996.
[45] A. P. Modi, « Effects of microstructure and experimental parameters on high stress abrasive wear behaviour of a 0.19wt% C dual phase steel », *Tribology International*, vol. 40, n° 3, p. 490‑497, mars 2007.
[46] C.-O. A. Olsson et M. Stemp, « Modelling the transient current from two rubbing electrode configurations: insulating pin on metal substrate and metal pin on insulating substrate », *Electrochimica Acta*, vol. 49, n° 13, p. 2145‑2154, mai 2004.
[47] N. Cabrera et N. F. Mott, « Theory of the oxidation of metals », *Rep. Prog. Phys.*, vol. 12, n° 1, p. 163, janv. 1949.
[48] E. J. W. Verwey, « Electrolytic conduction of a solid insulator at high fields The formation of the anodic oxide film on aluminium », *Physica*, vol. 2, n° 1‑12, p. 1059‑1063, janv. 1935.
[49] K. J. Vetter et F. Gorn, « Kinetics of layer formation and corrosion processes of passive iron in acid solutions », *Electrochimica Acta*, vol. 18, n° 4, p. 321‑326, avril 1973.
[50] B. A. Okorie, « Kinetics of Formation of Passive Oxide Films on Corrosion-Resistant Fe-Cr Thin Films », *Journal of The Electrochemical Society*, vol. 130, n° 2, p. 290, 1983.
[51] C.-O. A. Olsson, D. Hamm, et D. Landolt, « Evaluation of Passive Film Growth Models with the Electrochemical Quartz Crystal Microbalance on PVD Deposited Cr », *Journal of The Electrochemical Society*, vol. 147, n° 11, p. 4093, 2000.
[52] J. R. Goldberg et J. L. Gilbert, « Electrochemical response of CoCrMo to high-speed fracture of its metal oxide using an electrochemical scratch test method », *Journal of Biomedical Materials Research*, vol. 37, n° 3, p. 421–431, 1997.
[53] G. Okamoto, « Passive film of 18-8 stainless steel structure and its function », *Corrosion Science*, vol. 13, n° 6, p. 471‑489, 1973.
[54] A. J. Smith, M. Stratmann, et A. W. Hassel, « Investigation of the effect of impingement angle on tribocorrosion using single impacts », *Electrochimica Acta*, vol. 51, n° 28, p. 6521‑6526, sept. 2006.
[55] D. Déforge, F. Huet, R. P. Nogueira, P. Ponthiaux, et F. Wenger, « Electrochemical Noise Analysis of Tribocorrosion Processes under Steady-State Friction Regime », vol. 62, n° 6, p. 514–521, juin 2006.
[56] H.-H. Strehblow, « Phenomenological and Electrochemical Fundamentals of Corrosion », in *Materials Science and Technology*, Wiley-VCH Verlag GmbH & Co. KGaA, 2006.
[57] N. Sato et M. Cohen, « The Kinetics of Anodic Oxidation of Iron in Neutral Solution I . Steady Growth Region », *J. Electrochem. Soc.*, vol. 111, n° 5, p. 512‑519, mai 1964.
[58] L. Zhang, D. D. Macdonald, E. Sikora, et J. Sikora, « On the Kinetics of Growth of Anodic Oxide Films », *J. Electrochem. Soc.*, vol. 145, n° 3, p. 898‑905, mars 1998.
[59] M. Stemp, S. Mischler, et D. Landolt, « The effect of contact configuration on the tribocorrosion of stainless steel in reciprocating sliding under potentiostatic control », *Corrosion Science*, vol. 45, n° 3, p. 625–640, mars 2003.
[60] Y. Beygelzimer, « Grain refinement versus voids accumulation during severe plastic deformations of polycrystals: mathematical simulation », *Mechanics of Materials*, vol. 37, n° 7, p. 753‑767, juill. 2005.
[61] N. Gao, C. T. Wang, R. J. K. Wood, et T. G. Langdon, « Tribological properties of ultrafine-grained materials processed by severe plastic deformation », *J Mater Sci*, vol. 47, n° 12, p. 4779‑4797, juin 2012.
[62] K. Kato, « Wear in relation to friction — a review », *Wear*, vol. 241, n° 2, p. 151‑157, juill. 2000.